Helium distribution in a mantle shear zone from the Josephine Peridotite

A. Recanati [a,b,*], M.D. Kurz [b], J.M. Warren [c], J. Curtice [b]

[a] Laboratoire de Geologie, Ecole Normale Superieure, UMR 8538, 24 rue Lhomond, 75231 Paris Cedex 5, France
[b] Marine Chemistry and Geochemistry, Clark Lab 421, Woods Hole Oceanographic Institution, Woods Hole, MA 02543, USA
[c] Geological and Environmental Sciences, Stanford University, 450 Serra Mall, Stanford CA 94305-2115, USA

ARTICLE INFO

ABSTRACT

A previous study of oceanic mylonites suggested that peridotite helium concentrations are correlated with the degree of high-temperature ductile deformation in the mantle. In order to test this result, this study combines helium measurements with characterization of the deformation state of harzburgite samples in a small (6 m width) ductile mantle shear zone from the Josephine Peridotite, Oregon, USA. All measurements were made by coupled in vacuo crushing and melting, demonstrating that most of the helium ($ > 80\%$) resides within the solid phases rather than fluid or melt inclusions. The present study confirms the influence of deformation on helium contents, but only at the highest shear strain ($\gamma > 20$) are helium contents significantly higher. The highest helium concentration, by roughly a factor of two, is found in the center-most sample, which also has grain size reduction by a factor of ~ 4. Dislocations and sub-grain boundaries are present in all samples and do not correlate with helium concentrations. Mineralogy also appears to have a negligible influence in this shear zone, as modal mineralogy is relatively homogeneous, with all samples being harzburgites. These observations suggest that the increase in helium concentration is related to grain size reduction, with grain boundaries proposed as an additional storage site for helium in the mantle.

The present data also characterize the isotopic composition of the Josephine Peridotite: $^3He/^4He = 6.7 \pm 0.2$ Ra ($n = 33$, between 6.3 and 7.1 Ra). The presence of cosmogenic ^3He in the matrix is indicated by the helium isotopic composition released by melting: $^3He/^4He = 8.5 \pm 0.3$ Ra ($n = 10$; from 7.9 to 10.9). This corresponds to an exposure age of 10 Kyr, which is approximately concordant with the end of the last glacial maximum. Very little radiogenic helium is present in the samples, suggesting extremely low uranium and thorium contents ($[U] < 0.3$ ppb). Helium isotope measurements in four samples outside the shear zone suggest that mineralogy and melt infiltration are also important factors for understanding helium storage in the mantle.

1. Introduction

Helium isotopes have been extensively used as tracers of mantle fluxes and heterogeneity. However, mantle geochemistry is restricted by the availability of appropriate/representative mantle samples. Most previous studies of helium have focused on zero-age basalts from mid-ocean ridges and ocean islands, particularly in submarine glasses that trap substantial quantities of mantle helium (e.g., Kurz and Jenkins, 1981; Graham, 2002). Peridotites are more difficult to analyze, because they are the depleted residues of melting and therefore contain lower concentrations of helium and other incompatible elements. There

have been studies of continental peridotite xenoliths, which are generally thought to represent lithospheric sources (e.g., Gautheron et al., 2002, 2005), and some studies of seafloor peridotites (Kumagai et al., 2003, 2008; Kurz et al., 2009). Ophiolites and orogenic peridotites represent easily accessible portions of exhumed mantle, but there have been very few helium studies, with the single exception of the Beimarang ophiolite, in Tibet (Ye et al., 2007).

A previous study of mylonites from oceanic transform faults suggested that mantle deformation might increase the helium concentration in peridotites (Kurz et al., 2009). The high helium concentrations in oceanic mylonites were interpreted as evidence for noble gas storage on crystal defect sites or on grain boundaries. Hiraga et al. (2003, 2004, 2007) suggested that grain boundaries constitute significant reservoirs of incompatible elements (e.g. Ca, Al), based on analysis of natural and synthetic aggregates of olivine and other mineral assemblages. They also presented thermodynamic models to predict element enrichment at interfaces. Baxter et al. (2007) developed an experimental

* Corresponding author at: Laboratoire de Geologie, Ecole Normale Superieure, UMR 8538, 24 rue Lhomond, 75231 Paris Cedex 5, France.
E-mail addresses: alice.recanati@gmail.com, arecanati@mnhn.fr (A. Recanati), mkurz@whoi.edu (M.D. Kurz), warrenj@stanford.edu (J.M. Warren), jcurtice@whoi.edu (J. Curtice).

procedure to measure noble gas (helium and argon) partitioning into grain boundaries. Their results also suggest that fine-grained materials would have higher helium and argon contents, although the influence of other crystal defects (e.g. dislocations) on helium retention or release is poorly understood (Baxter, 2010). Alternatively, a mineralogical control on the high helium abundances in oceanic mylonites could not be ruled out in the study by Kurz et al. (2009).

In order to test the relationship between mantle deformation and helium contents, and to evaluate the suitability of ophiolites for helium isotope studies, we analyzed samples from a high temperature shear zone in the Josephine Peridotite, Oregon, USA. The main focus of this study is one of the narrowest of the ∼10 shear zones exposed in the ∼1 km wide Fresno Bench section of the Josephine Peridotite. This shear zone is approximately 6 m wide, and is referred to here as shear zone A. This site was also chosen to eliminate mineralogy as a dominant factor, as the shear zone is relatively homogeneous with respect to mineralogy, being composed of spinel harzburgite with minor variations in orthopyroxene abundance.

2. Sampling

The Josephine Peridotite is a Jurassic-age mantle section that is one of several coast range ophiolites in southwest Oregon and northwest California (Fig. 1). This peridotite is the remnant of either a back-arc basin (Harper, 1984) or a fore-arc setting (Dick, 1976; Kelemen and Dick, 1995), emplaced at 157 Ma (Saleeby et al., 1982). It is an exceptionally well exposed, 800 km^2 massif, predominantly composed of harzburgite, and has been extensively studied to understand mantle melting and melt extraction processes (Himmelberg and Loney, 1973; Dick, 1976; Kelemen and Dick, 1995; Harper, 1984, 2003; Harper et al., 1994, Sundberg et al., 2010). This mantle section has been heterogeneously deformed, leading to the formation of several small ductile shear zones, which outcrop over 1 km in the Fresno Bench area near Vulcan Peak. The shear zones are characterized by a vertical transposition of originally sub-horizontal layers, defined by variations in orthopyroxene content, and vary in width between 1 and 60 m (Kelemen and Dick, 1995; Warren et al., 2008). These shear zones are ideal for field study, since the orientation of the orthopyroxene foliation planes are relatively easy to observe and can be used to calculate shear strain (Warren et al., 2008). Previous field studies have used the Josephine shear zones to study the rheology of ductile-deformed olivine (Warren et al., 2008; Skemer et al., 2010).

The focus of this study is shear zone A, which is on the southwest side of Fresno Bench at 42° 10.325′N, 123° 58.817′W and approximately ∼1236 m elevation. The orientation of shear zone A was measured in the field to be 045/90, with a lineation 50/045. Ten oriented samples were collected along a 15 m transect approximately perpendicular to the shear plane. All samples are harzburgite, which forms >90% of the Josephine Peridotite (Dick, 1977). They are composed of ∼60–70% olivine, ∼30% orthopyroxene, <1% clinopyroxene, and 0.5–2% spinels. In most samples, clinopyroxene is rare or absent. Orthopyroxenes define the sample foliation and are easily observed on the outcrop because of surficial oxidation and preferential weathering of olivine.

A map of the shear zone, projected into the kinematic X–Z reference frame, is shown in Fig. 1. The structural X–Z plane is perpendicular to the shear plane (315/50) and aligned with the shear direction (Z=0). At the edge of the shear zone (Z > ± 3 m),
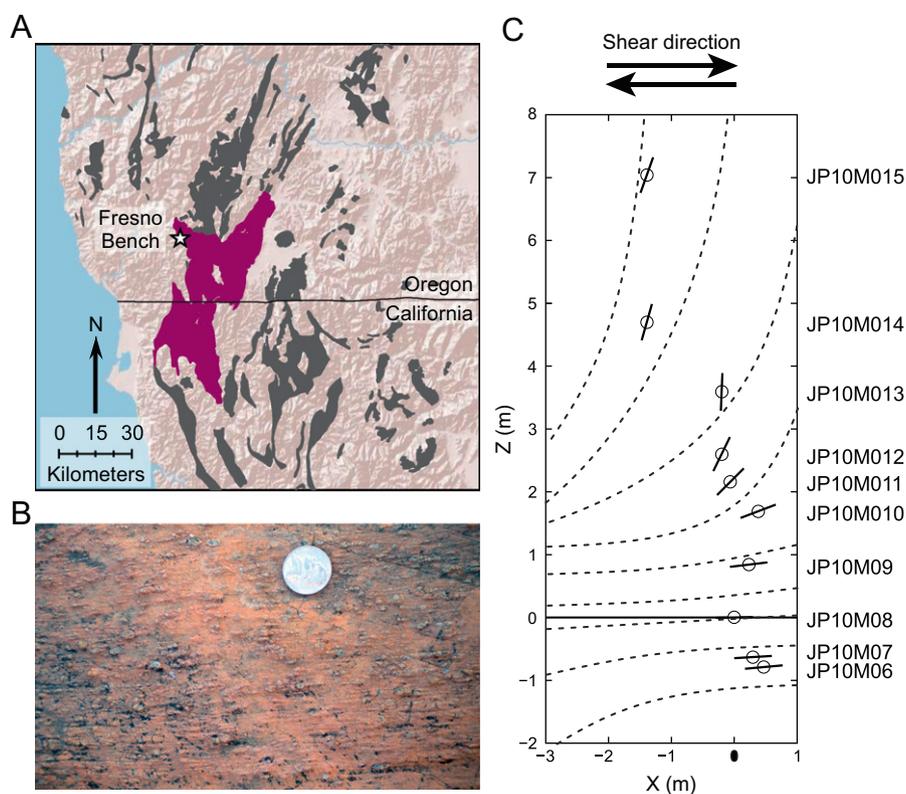
Fig. 1. Sample location and X–Z cross-section of shear zone A: regional map indicating the location of the Fresno Bench section of the Josephine Peridotite (A); photograph of the center-most sample of shear zone A (JP10M08), including orthopyroxene lineation (B); X–Z cross section of shear zone A (C). Sample locations are represented by circles, measured pyroxene foliations by short lines, and the shear plane by a long black line. Dashed lines represent a schematic drawing of the shear zone based on the measured pyroxene foliations. This map is a projection onto the X–Z plane, perpendicular to the shear plane (315/50) and aligned with the shear direction (Z=0).

samples are moderately deformed, and the foliation and lineation are almost perpendicular to the shear plane/shear direction. Close to the shear zone center ($|Z| < 1$), the foliation and lineation are parallel to the shear plane/shear direction.

In addition to systematic sampling across the shear zone, this study includes several coarse-grained, undeformed samples that were collected within ~50 m of shear zone A. These samples represent the different mineralogies found within the Josephine Peridotite, and are included here to provide a broader context for the shear zone samples. Sample JP10M01 is a chromitite vein in a dunite pod within harzburgite. Sample JP10M02 is a pyroxenite sample from a 10–20 cm wide vein inside a clinopyroxene-bearing harzburgite (JP10M04). These two samples are within 0.5 m of each other in the field. The harzburgite has a relatively high abundance of clinopyroxene (~4–5%) for the Josephine Peridotite, which may be due to melt percolation related to the pyroxenite vein. JP10M05 is a separate 6 cm wide clinopyroxenite vein in harzburgite. These samples and veins are related to melt transport in the peridotite, which is interpreted to have occurred before, during, and after deformation at Fresno Bench (Kelemen and Dick, 1995).

3. Methods

This study combines helium measurements with deformation analysis of samples from shear zone A, including shear strain calculation, grain size measurement and textural analysis. The methodology used to characterize deformation in the samples follows that of previous studies of the Fresno Bench shear zones (Warren et al., 2008; Skemer et al., 2010), as well as sample oxidation to study olivine dislocation populations. The helium measurements were performed following the experimental procedure and mass spectrometry techniques previously reported by Kurz et al. (1990, 2004, 2009).

Assuming that volume change did not occur, displacements within the shear zone are only due to deformation by simple shear (Ramsay and Graham, 1970; Warren et al., 2008). The deflection of the orthopyroxene foliation was used as a marker for shear strain, γ (Fig. 1), assuming $\gamma = 0$ for the sample furthest from the shear zone center (JP10M15). Samples were reoriented in the laboratory, and thin sections were cut in the X–Z plane (315/50) perpendicular to the shear plane. Grain size measurements were performed by the mean line intercept technique on 300 grains per sample for seven samples, applying a stereographic correction factor of 1.5 (Underwood, 1970; Drury, 2005; Warren et al., 2008). Four thin sections were decorated using the Kohlstedt et al. (1976) method in order to examine olivine dislocation structure. This method results in the selective oxidation of lattice dislocations, which can be imaged using either a petrographic microscope or a scanning electron microscope. In this study, it was used in an attempt to determine if dislocation abundance correlates with helium content in the peridotites.

For noble gas analysis, samples were lightly crushed in a stainless steel mortar and pestle, and three fractions were hand-picked using a binocular microscope. Chips of >2 mm size were used for whole rock measurements and, whenever possible, olivine and orthopyroxene from the 1–2 mm size fraction were separated. The orthopyroxene fraction is composed of non-altered orthopyroxene macroscopic crystals. The olivine fraction is composed of multiple olivine grains, avoiding major oxidation and larger chromite or magnetite inclusions (i.e. >100 μm). In the most deformed sample, JP10M08, it was impossible to make an orthopyroxene separate due to the small grain size. Mineral separates were prepared from the 0.5–1 mm size fraction for three samples, using a Frantz magnetic separator, in order to

eliminate separation technique and grain size as influences on the helium measurements. Mineral separates were also prepared from harzburgite sample JP10M04 (olivine, orthopyroxene, clinopyroxene), because clinopyroxene was more abundant than in the shear zone samples.

All samples were analyzed by coupled in vacuo crushing and melting, to document the distribution of helium within the rocks and minerals. Numerous blanks and standards were run along with the samples, with at least 10 air standards and blanks typically run over the course of a single day. Concentrations and isotopic compositions are reported relative to air standards. The error in $^3He/^4He$ was computed as a function of the error in the blanks and standards, and is generally 1–2%. The analytical error in ^4He is ~1%, i.e. the quadrature sum of the uncertainty in the blank (~2.8×10^{-12} ccSTP/g) and the reproducibility of standards ($<1\%$). Repeat measurements of several samples yielded larger variability (~7% for sample JP10M08, $n = 3$). This variability was included in the estimate of the ^4He uncertainties, yielding ~7%, which is a conservative estimate because it combines both analytical uncertainties with an estimate of reproducibility of individual samples. These conservative uncertainties are included in Table 1 and represented as ^4He error bars in all figures. The experimental procedure and helium mass spectrometry have been previously documented (Kurz et al., 2004, 2009).

4. Results

4.1. Microstructural evolution of shear zone A

The angle between the foliation plane and the shear plane decreases from 70° at the edge of the shear zone to 1° at the center. This corresponds to a variation in calculated shear strain from $\gamma = 0$ to $\gamma = 64$ (Fig. 2A, Table 1), assuming that the sample the furthest from the shear plane (JP10M15) represents zero shear strain. The main uncertainty in this calculation is the choice of the reference "unstrained" sample. However, taking either JP10M13, 14, or 15 as the unstrained sample results in $<1\%$ difference in the calculated strain for the most deformed sample. The center-most sample has a significantly higher shear strain than all the other samples, due to shear localization in the central 1 m wide portion of the shear zone (Fig. 1).

Samples from the edge of the shear zone are coarse-grained harzburgite, mostly composed of 1–3 mm round orthopyroxene

Table 1
Background information: Results from grain size measurements, shear strain calculation, and trace element analyses, where "nd" and "na" respectively denote not determined and not applicable. Uranium and thorium concentrations were determined from whole rock inductively-coupled plasma mass spectrometer measurements, analyzed at WSU Geoanalytical Lab. DST-1 is an analytical dunite standard, referenced by Govindaraju (1994).

	Z (m)	Grain size (μm)	Shear strain	U (ppm)	Th (ppm)
JP10M15	7.0	838	0	nd	nd
JP10M14	4.7	797	0	0.0118	0.04
JP10M13	3.6	1022	0	nd	nd
JP10M12	2.6	780	0	0.0105	0.05
JP10M11	2.2	nd	1	nd	nd
JP10M10	1.7	nd	2	nd	nd
JP10M09	0.8	642	8	nd	nd
JP10M08	0	289	64	0.0101	0.04
JP10M07	-0.6	nd	17	nd	nd
JP10M06	-0.8	482	11	0.0081	0.03
JP10M05	na	nd	na	0.0130	0.04
DTS 1	na	na	na	0.0175	0.04
DTS 1-Govindaraju	na	na	na	0.0036	0.01

porphyroclasts in a coarse-grained euhedral olivine matrix (Fig. 3A). From the edge to the center of the shear zone (i.e. as strain increases), the mean grain size decreases from 1 mm to 289 μm (Fig. 2B, Table 1) and the grains become stretched with a shape-preferred orientation (Figs. 3,4). Across the center of the shear zone, there is a large variation of shear strain, grain size, and texture between the center-most sample (JP10M08, Fig. 3C) and

the next closest samples, which are 0.5 m away (JP10M07, JP10M06, Fig. 3B). The highest strain sample, JP10M08, is fine-grained (mean grain size of 289 μm), with a strong stretching lineation in the shear direction and a low proportion of orthopyroxene porphyroclasts. The microstructure of this sample is heterogeneous, with coexisting coarser-grained bands (> 300 μm) that are strongly stretched and finer-grained domains (< 100 μm) that are recrystallized (Fig. 3C).
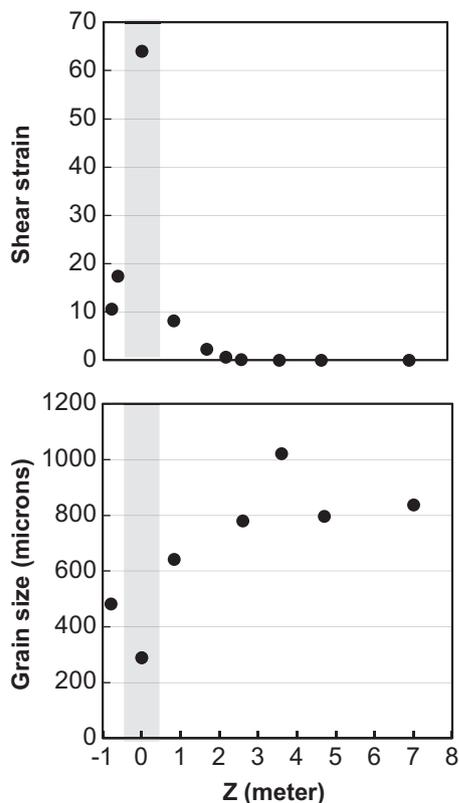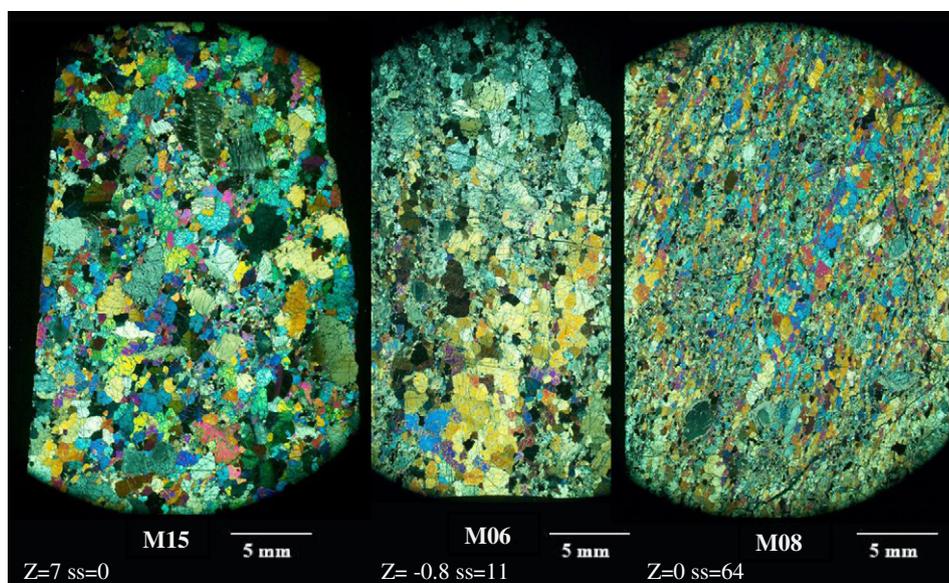
4.2. Helium in shear zone A

4.2.1. Helium contents

Table 2 presents crushing and melting results. Among the Josephine Peridotite samples, only 4–21% of the total helium is released by crushing. Therefore, helium does not reside in bubbles, fluid, or melt inclusions that are larger than 93 μm, the median grain size of the crushed powder (Kurz et al., 2009). Microscopic examination of individual olivine grains from the 355–500 μm fraction of JP10M14 and the 212–250 μm fraction of JP10M08 failed to reveal any fluid or melt inclusions, up to a magnification of $300 \times$. Therefore, it is unlikely that fluid or melt-inclusions in olivine, if present, are larger than 10–15 μm. Inclusions below 10 μm cannot be excluded and could contribute to the helium released during the melting step.

Except for the center-most sample, helium contents are relatively constant across the shear zone (Fig. 5A), with a median value of $^4He_{tot} = 56 \pm 26$ nccSTP/g ($n = 10$, whole rock measurements). The single sample at the center of the shear zone (JP10M08) has a higher helium concentration ($^4He_{tot} = 120 \pm 10$ nccSTP/g, $n = 3$), which is more than twice the median helium concentration of the other samples, and is significantly higher at the 95% level of confidence.

4.2.2. Helium isotopes

The values of $^3He/^4He$ obtained by crushing are constant within the whole rocks and mineral separates (Fig. 5B): $^3He/^4He = 6.6 \pm 0.3$ Ra for whole rocks ($n = 10$); $^3He/^4He = 6.7 \pm 0.3$ Ra both for olivine ($n = 8$), and for orthopyroxene ($n = 7$). The $^3He/^4He$ values obtained by melting experiments in this study are always higher than the crushing values ($^3He/^4He = 8.5 \pm 0.3$ Ra, $n = 10$).

Fig. 2. Variability in calculated shear strain and measured grain size across shear zone A: Z is the distance from JP10M08 (the assumed center of shear zone A), measured perpendicularly to the shear plane. The gray shaded box indicates the center part of the shear zone ($|Z| < 50$ cm).

Fig. 3. Photomicrographs illustrating the microstructural evolution across shear zone A: the thin sections are cut on the X–Z plane (315/50), top to the north. Photomicrographs were taken in cross-polarized light and ss denotes shear strain. From left to right: samples JP10M15, JP10M06, and JP10M08.

Table 2
Helium results: Whole rock (wr), olivine separates (olv), orthopyroxene separates (opx), and clinopyroxene separates (cpx) results. Outside shear zone A (SZA): chromite (Chr.), pyroxenite (Pyr.), harzburgite (Harz.), and clinopyroxenite (Cpxit.).

Sample		Crush					Melt				Total		
		Size (mm)	^{4}He (ncc/g)	±	^{3}He/^{4}He (Ra)	± (Ra)	^{4}He (ncc/g)	± (ncc/g)	^{3}He/^{4}He (Ra)	± (Ra)	^{4}He (ncc/g)	± (ncc/g)	Fraction crushed
JP10M15	wr	> 2	4.8	0.3	6.84	0.12	47.4	3.3	8.90	0.12	**52.5**	3.3	0.09
JP10M15	olv	1 − 2	8.9	0.6	6.71	0.11	49.2	3.4	9.04	0.12	**58.9**	3.5	0.15
JP10M15	opx	1 − 2	5.8	0.4	6.98	0.13	53.6	3.8	8.88	0.12	**59.7**	3.8	0.10
JP10M14	wr	> 2	3.9	0.3	6.39	0.13	22.6	1.6	10.95	0.17	**26.8**	1.6	0.15
JP10M14	olv	1 − 2	3.8	0.3	6.42	0.14	23.2	0.2	10.87	0.16	**27.5**	1.6	0.14
JP10M14	olv	1 − 2	4.6	0.3	6.31	0.12	24.7	1.7	10.60	0.15	**29.6**	1.8	0.16
JP10M14	opx	1 − 2	2.8	0.2	6.72	0.17	12.8	0.9	15.08	0.23	**15.7**	0.9	0.18
JP10M14	opx	0.5 − 1	1.9	0.1	6.60	0.19	13.7	1.0	14.28	0.22	**15.8**	1.0	0.12
JP10M13	wr	> 2	7.5	0.5	6.60	0.12	48.5	3.4	8.14	0.11	**56.8**	3.4	0.13
JP10M13	olv	1 − 2	4.4	0.3	6.57	0.13	31.0	2.2	9.45	0.13	**35.8**	2.2	0.12
JP10M13	opx	1 − 2	24.0	1.7	6.65	0.10	109.8	7.7	7.07	0.10	**135.1**	7.9	0.18
JP10M12	wr	> 2	6.0	0.4	6.41	0.12	60.7	4.3	8.16	0.11	**67.1**	4.3	0.09
JP10M12	opx	1 − 2	14.3	1.0	6.83	0.11	91.6	6.4	7.90	0.11	**106.4**	6.5	0.13
JP10M09	wr	> 2	5.2	0.4	6.63	0.13	49.1	3.4	8.29	0.11	**54.7**	3.5	0.10
JP10M09	olv	1 − 2	3.7	0.3	6.75	0.14	45.3	3.2	8.37	0.12	**49.3**	3.2	0.08
JP10M09	olv	0.5 − 1	3.4	0.2	6.85	0.14	48.3	3.4	8.38	0.11	**51.9**	3.4	0.07
JP10M09	opx	0.5 − 1	6.9	0.5	6.32	0.12	55.0	3.9	8.23	0.11	**62.7**	3.9	0.11
JP10M08	wr	> 2	6.1	0.4	6.52	0.12	118.3	8.3	7.26	0.09	**124.9**	8.3	0.05
JP10M08	wr	> 2	4.6	0.3	6.47	0.14	104.6	7.3	6.84	0.10	**109.7**	7.3	0.04
JP10M08	wr	> 2	5.5	0.4	6.56	0.12	115.3	8.1	7.16	0.09	**121.1**	8.1	0.05
JP10M08	olv	0.5 − 1	2.7	0.2	6.56	0.16	112.7	7.9	7.03	0.09	**115.8**	7.9	0.02
JP10M07	wr	> 2	7.4	0.5	6.65	0.12	49.2	3.4	8.60	0.12	**56.9**	3.5	0.13
JP10M07	olv	1 − 2	2.2	0.2	6.61	0.16	25.0	1.7	10.28	0.14	**27.3**	1.8	0.08
JP10M07	opx	1 − 2	17.5	1.2	6.78	0.11	65.3	4.6	8.53	0.12	**84.2**	4.7	0.21
JP10M06	wr	> 2	5.4	0.4	6.76	0.14	48.5	3.4	8.04	0.11	**54.1**	3.4	0.10
JP10M06	olv	1 − 2	5.6	0.4	6.82	0.13	42.1	2.9	8.46	0.12	**47.9**	3.0	0.12
JP10M06	opx	1 − 2	7.0	0.5	6.54	0.12	54.8	3.8	8.24	0.11	**62.1**	3.9	0.11
Outside SZA													
JP10M01	Wr Chr.	> 2	78.1	5.5	6.74	0.09	259.9	18.2	6.88	0.12	**345.3**	19.0	0.23
JP10M02	Wr Pyr.	> 2	25.7	1.8	6.85	0.10	145.8	10.2	7.74	0.13	**172.6**	10.4	0.15
JP10M04	Wr Harz.	> 2	12.0	0.8	6.65	0.10	124.6	8.7	7.34	0.13	**137.3**	8.8	0.09
JP10M04	Olv Harz	0.5 − 1	11.2	0.8	6.75	0.11	111.9	7.8	7.35	0.09	**123.6**	7.9	0.09
JP10M04	Opx Harz	0.5 − 1	8.0	0.6	6.73	0.12	88.3	6.2	7.57	0.09	**96.6**	6.2	0.08
JP10M04	Cpx Harz	5 − 1	16.5	1.2	6.49	0.10	175.5	12.3	6.99	0.08	**193.1**	12.3	0.09
JP10M05	Wr Cpxit	> 2	378.8	26.5	6.48	0.08	1153.4	80.7	6.05	0.11	**1548.8**	85.0	0.24
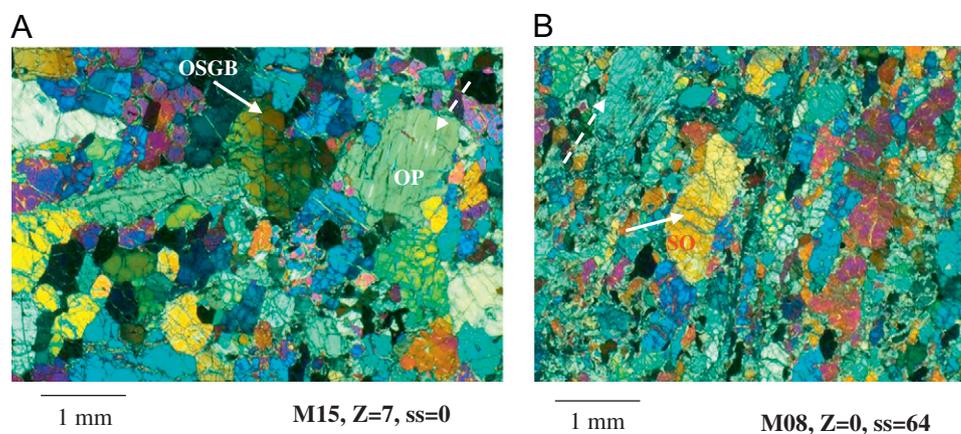
Fig. 4. Photomicrographs illustrating changes in fabrics across SZA: (A) Sample JP10M15. White solid arrow indicates olivine with sub-grain boundaries (OSGB) due to previous deformation and white dashed arrow indicates an orthopyroxene porphyroclast (OP). (B) Sample JP10M08. White solid arrow indicates a stretched olivine (SO) in a coarser-grained band and dashed arrow indicates a stretched Opx grain.

The higher ^{3}He/^{4}He obtained during the melting stage of the measurements suggests the presence of cosmogenic ^{3}He in the matrix of samples, as found in basaltic phenocrysts (Kurz, 1986). The absence of any samples with ^{3}He/^{4}He < 7.0 Ra during the melting stage of the measurements suggests that relatively little

radiogenic helium is bound up within minerals, as radiogenic production would have significantly decreased ^{3}He/^{4}He due to the low radiogenic production ratio (^{3}He/^{4}He < 0.1 Ra). The respective contributions of cosmogenic, radiogenic, and mantle helium are discussed further below.
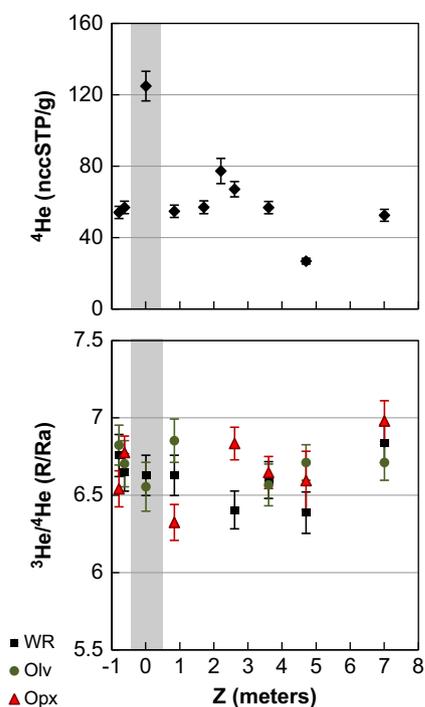
Fig. 5. Variability in helium contents and isotopic composition across shear zone A: ^{4}He is the total ^{4}He concentrations from whole rock measurements. Error bars are calculated from the error in the blank and a 7% error based on the reproducibility of sample JP10M08. ^{3}He/^{4}He was obtained by crushing whole rocks (squares), olivines (circles), and orthopyroxenes (triangles). Error bars only take into account the blank error ($\sim$0.15), since the reproducibility error is significantly smaller.

Whole rock, olivine, and orthopyroxene have the same ^{3}He/^{4}He signature, as confirmed by the measurement of six olivine/orthopyroxene pairs. Orthopyroxene has higher helium contents than coexisting olivine (^{4}He$_{opx}$/^{4}He$_{ol}$=1–4), except for sample JP10M14 (^{4}He$_{opx}$/^{4}He$_{ol}$=0.5).

4.3. Helium in nearby chromitite and pyroxenite veins

The samples collected outside shear zone A are undeformed samples and also differ from the shear zone samples in mineralogy. Sample JP10M01 is a chromitite composed of mm-size euhedral chromite crystals, while JP10M02 is a pyroxenite. JP10M04 is a coarse-grained ($\sim$1–3 mm) grained clinopyroxene-bearing harzburgite. Clinopyroxenite JP10M05 is composed of large (centimeter-sized) euhedral clinopyroxene crystals, oriented parallel to the vein edges.

The pyroxenite dike (JP10M02) has a slightly higher helium content of ^{4}He$_{tot}$=170 $\pm$ 10 nccSTP/g, compared to the adjacent harzburgite (JP10M04). It is noteworthy that the clinopyroxenite vein (JP10M05), composed of > 90% clinopyroxene, has ^{4}He$_{tot}$=1500 $\pm$ 100 nccSTP/g, which is the highest helium content in any of the samples studied here. The chromitite vein (JP10M01) also has a relatively high helium content: ^{4}He$_{tot}$=350 $\pm$ 10 nccSTP/g. The clinopyroxene-bearing harzburgite (JP10M04) has a helium content of ^{4}He$_{tot}$=140 $\pm$ 10 nccSTP/g. This value is 2.5 times higher than the median of shear zone A samples. Comparison of Cpx and Opx indicates that ^{4}He$_{CPX}$/^{4}He$_{OPX}$=2, while the helium content of the orthopyroxene separate is slightly lower than the olivine separate. The isotopic composition of the samples collected outside shear zone A is constant and similar to the shear zone samples, with an average value of ^{3}He/^{4}He=6.7 $\pm$ 0.3 Ra (n=7).

5. Discussion

5.1. Effect of mineralogy on helium storage

Shear zone A was partially chosen to focus on the influence of deformation processes and to eliminate mineralogical differences, as all samples are harzburgites. The center-most sample of the shear zone (JP10M08) has the highest helium concentration (Fig. 5), but is mineralogically similar to other samples from the shear zone. This suggests that mineralogy is not the cause of this increased helium abundance. In this sample (JP10M08), the high helium concentration in the olivine mineral separate (^{4}He$_{ol}$=116 $\pm$ 8 nccSTP/g) indicates that the high bulk He concentration (^{4}He$_{tot}$=120 $\pm$ 10 nccSTP/g) is not due to an increased orthopyroxene modal abundance.

Among all the samples, helium concentrations in olivine and orthopyroxene are generally consistent with whole rock helium concentrations. Using a harzburgite modal mineralogy of 75% olivine and 25% orthopyroxene, calculated bulk rock concentrations differ from whole rock measurements by less than 13%, except for sample JP10M07 (27%). For example, JP10M06 has ^{4}He$_{ol}$=48 $\pm$ 3 nccSTP/g and ^{4}He$_{opx}$=62 $\pm$ 4 nccSTP/g, which corresponds to a calculated bulk rock concentration of ^{4}He=52 $\pm$ 2 nccSTP/g. This differs by only 5% from the measured bulk ^{4}He$_{tot}$=54 $\pm$ 3 nccSTP/g. The difference between calculated and measured bulk rock concentrations is generally within the range of analytical error and demonstrates that olivine and orthopyroxene are the dominant helium residence sites in these rocks.

Other minerals present in shear zone A (clinopyroxene, spinel and serpentine) do not control whole rock helium contents as they are either present in low abundance and/or have low concentrations. Thin section observations confirm that whole rock helium concentrations are not directly related to the extent of serpentinization. For instance, JP10M08 and JP10M14 both have $\sim$4% serpentinization whereas helium concentrations vary by a factor of 5. Additionally, available data from serpentine veins (from Kurz et al., 2009) indicate that serpentine has very low helium concentrations (< 10 nccSTP/g). Thus, slight variations in serpentine abundance (1–4%) cannot be involved in the increased helium concentration in JP10M08.

The partitioning between olivine and orthopyroxene in the Josephine harzburgites indicates that orthopyroxene/olivine partitioning ranges from 0.5 to 3.8 (n=7), and is > 1 for all samples except JP10M14. For comparison, one olivine/orthopyroxene phenocryst pair in a Hawaiian (Mauna Kea) shield lava yielded the opposite partitioning behavior, with ^{4}He$_{opx}$/^{4}He$_{ol}$=0.1 (Kurz et al., 2004), but they may be xenocrysts derived from different melts. The slightly higher concentration of He in pyroxenes results in higher He concentrations for pyroxenite compared to harzburgite. The pyroxenite dike (JP10M02) contains $\sim$45% orthopyroxene and has ^{4}He=172 nccSTP/g, while harzburgite ($\sim$25% orthopyroxene) has helium concentrations of 26–137 nccSTP/g.

The influence of clinopyroxene on helium storage can be estimated from the clinopyroxenite vein and the clinopyroxene-bearing harzburgite. The clinopyroxenite vein (> 90% clinopyroxene) has an extremely high helium concentration (1536 nccSTP/g). Additionally, the clinopyroxene-bearing harzburgite (JP10M04) also has a relatively high helium content (172 nccSTP/g) compared with clinopyroxene-poor samples (26–137 nccSTP/g).

5.2. Effect of cracking on helium storage

During alteration and emplacement of peridotites, cracking of grains has the potential to result in helium loss from grain boundaries and grain matrices. In theory, microcracks are initiated at grain boundary triple junctions in polycrystalline

materials when a critical grain size is exceeded (Evans, 1978). Depending on their density and geometry, microcracks can result in increased stress levels, causing intergranular crack propagation. This is likely to occur at low confining pressures and for large temperature variations, and may result in an interconnected crack network (deMartin et al., 2004). Low-temperature fluid flow through this crack network then allows serpentinization to occur.

Observation of the shear zone A samples indicates that minimal thermal cracking occurred (Fig. 3). Using the highest magnification of the optical microscope ($\sim$1–2 µm resolution), olivine–olivine grain boundaries appear tight, with no grain boundary cracks or serpentine networks along grain boundaries. Shear zone A harzburgite samples are weakly altered, with only a few percent serpentinization. When present, serpentine fills cm-long veins or cracks cross-cutting grains. Veining is oriented differently from shear direction and is thus later than ductile deformation. Fractures are typically <1 mm wide, with minor variability in fracture density among samples. Therefore, cracking in the Josephine samples appears to have been driven by the volume increase associated with serpentine formation, not by thermal cracking.

Helium release due to cracking cannot be fully excluded in the Josephine samples. However, the low microcrack and serpentine vein density in the Josephine samples suggests that cracking is relatively unimportant. Overall, petrographic observation reveals no correlation bewteen variations in helium concentration and microcrack abundance.

### 5.3. Effect of ductile deformation on helium

5.3.1. Deformation and helium contents

Temperature conditions during deformation in the Fresno Bench area have been previously constrained as approximately 1000 °C (Harding, 1988; Loney and Himmelberg, 1976; Kelemen and Dick, 1995; Skemer et al., 2010). At this temperature and at the grain sizes present in most Josephine samples, deformation occurs predominantly by dislocation creep in the ductile regime (Hirth and Kohlstedt, 2003; Warren et al., 2008; Skemer et al., 2010). The absence of ultramylonite in the Fresno Bench shear zones suggests lower strain and possibly lower strain rates than larger shear zones such as oceanic transforms faults and shear zones in the Oman Ophiolite, where ultramylonites are observed (e.g., Boudier et al., 1988; Jaroslow et al., 1996). The most deformed sample collected from shear zone A (JP10M08) is closer to a protomylonite in texture than a mylonite. The grain size is only reduced by a factor of 4 and this sample does not appear to have transitioned to the diffusion creep regime, based on the presence of an olivine lattice preferred orientation.

Despite the absence of ultramylonites, strain localization has occurred in the Josephine shear zones. The central 1 m of the shear zone has high shear strains ($\gamma > 20$) that result in large differences in texture and microstructure between JP10M08 and the closest samples (Fig. 3). The helium distribution across shear zone A reveals that the highest strained sample has the highest helium concentration (Fig. 6), thus supporting a relationship between texture, grain size, and helium content. Note that three replicate helium measurements of sample JP10M08 were performed, all yielding similar high helium contents (110–125 nccSTP/g).

5.3.2. Helium storage on grain interfaces

Several existing models and experiments support the suggestion that high helium concentrations in deformed peridotites could be due to increased grain boundary storage. Hiraga et al. (2002, 2003, 2004, 2007), Hiraga and Kohlstedt (2007, 2009) and Baxter et al. (2007) all suggested that crystal defects influence
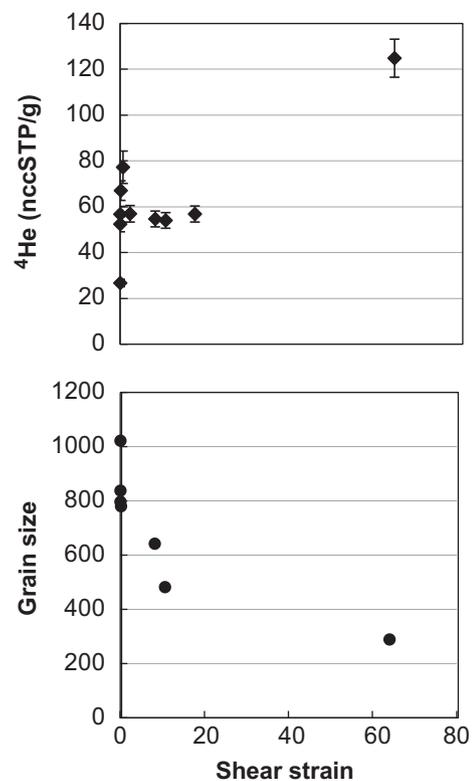

Fig. 6. Relationship between shear strain and helium contents: ^{4}He is the total ^{4}He concentration from whole rock measurements. Shear strain was computed from the deflection of the orthopyroxene foliation. Strain localization results in an increased helium concentration in the center of shear zone A.

elemental residence sites, in addition to mineralogy and fluid or melt inclusions. From a mineral physics perspective, grain and interphase boundaries are types of crystal defects, visible at the microscopic scale. Intraphase grain boundaries are by definition a misorientation of 10° or more in the crystal lattice of a phase. Interphase boundaries are the interfaces between different mineral phases, corresponding to both a compositional and structural mismatch in the crystal lattice.

Hiraga et al. (2004) demonstrated that grain-interfaces can be significant reservoirs of incompatible elements in the mantle. They proposed a thermodynamic model for the equilibrium partitioning of trace elements between grain matrices and grain boundaries. In this treatment, grain boundaries are considered phases in their own right, with a width corresponding to the zone of lattice distortion at the interface between two grains, typically 0.75 nm (Hiraga and Kohlstedt, 2009). Hiraga et al. (2004, 2007) predicted that a significant volume of noble gases could reside at equilibrium in grain boundaries. Thus, grain size reduction would increase the total storage capacity for highly incompatible elements, due to the increase in grain interfaces at smaller grain sizes. Baxter et al. (2007) presented experimental data for the partitioning of noble gases onto grain boundaries in diopside aggregates. Pinilla et al. (2012) recently calculated the favorable incorporation energy for noble gases on grain boundaries.

In shear zone A, helium concentrations are significantly increased only in the finest-grained sample (grain size of 285 µm). However, the relative storage capacity of grain boundaries depends on the grain boundary volume relative to the grain matrix volume. Considering a distribution of equally shaped grains with a constant grain boundary width (w), the average relative grain boundary volume is proportional to w/d, where d is the average grain size. Terwilliger and Chiang (1995) and Hiraga et al. (2007) computed relative grain boundary volume by modeling grains as tetrakaidecahedrons, the
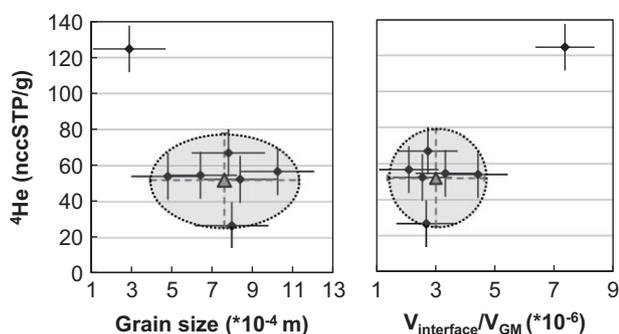
Fig. 7. Helium contents as a function of the grain size and the relative grain interface volume: Sample JP10M08 has significant increase both in ^{4}He and V_{int}/V_{GM}. The ratio of interstitial volume to the grain matrix was calculated from the 2D grain size measurements, using equation (4) from Hiraga and Kohlstedt (2009). This assumes tetrakaidecahedron grain shape, a log normal grain size distribution, and a 0.75 nm grain boundary width. ^{4}He is the total ^{4}He concentration from whole rock measurements. The gray-filled triangle represents the average value for all samples except JP10M08. The black error bars represent the standard deviation among these six samples (σ). Dashed gray error bars correspond to $2 \times \sigma$. Assuming a log-normal repartition, the gray-filled dashed ellipse represents a 95% uncertainty ellipse for these samples.

closest mathematical approximation for an equant grain shape. Using equation 4 from Hiraga and Kohlstedt (2009), the volume of grain boundaries (V_{int}) is related to the volume of grain matrices (V_{gm}) by the expression:

$$V_{int}/V_{gm} = 2.84 \times w/d$$

where w is the grain boundary width (typically assumed to be 0.75 nm) and d is the average measured grain size. This formula provides values of the relative proportion of grain boundaries to grain matrix volume V_{int}/V_{gm} on the order of 10^{-6}.

In this study, out of seven measured samples, the most deformed sample (JP10M08) has a significant grain size reduction, corresponding to $V_{int}/V_{gm} = 7 \times 10^{-6}$, combined with a significant increase in helium concentration (^{4}He = 125 nccSTP/g). The variation in grain size among the six other samples is less than a factor 2 (Fig. 7), corresponding to an average value for V_{int}/V_{gm} of $3 \times 10^{-6} \pm 1 \times 10^{-6}$. In these six samples, the average helium concentration is ^{4}He = 52 ± 13 nccSTP/g. Thus, sample JP10M08 has an increase in both V_{int}/V_{GM} and helium concentration compared to the other samples (Fig. 7).

The ratio of JP10M08 to the average value of other samples for V_{int}/V_{gm} is 2.4 ± 0.7 and for ^{4}He is 2.5 ± 1. Calculation of these two values is entirely independent. The similar enrichment factors suggest that increased grain boundary volume directly corresponds to increased He storage. Note also that these factors do not depend on the value of the grain boundary width. Therefore, grain boundary storage appears to be a dominant factor in controlling helium storage among fine-grained peridotites.

The amount of helium expected to be stored on grain boundaries is difficult to calculate, as helium partition coefficients between crystal lattice and grain boundaries are not well constrained. Baxter et al. (2007) measured grain boundary partitioning of helium and argon at equilibrium in synthetic melt-free polycrystalline diopside aggregates, by first irradiating samples and then measuring noble gas release during step heating experiments. For helium, ^{4}He released in the temperature range 150–400 °C was assumed to represent helium stored on grain boundaries, while helium released at temperature > 750 °C was assumed to represent helium from grain interiors. From this, Baxter et al. (2007) determined helium mass ratios in grain boundaries/grain interiors ($R = m_{int}/m_{GM}$), resulting in an average partition coefficient $R = 6 \pm 14$ ($n = 17$). Application of such partitioning data to shear zone A samples is speculative as these

samples are not diopside aggregates, and may not be at equilibrium. However, the average partitioning coefficient $R = 6$ implies that the quantity of helium stored at interfaces is not negligible compared to both the quantity stored in grain matrices and the total bulk quantity. Baxter concluded that for grain sizes < 1 mm, melt-free grain boundaries could retain significant proportions of the bulk rock helium, which is consistent with our hypothesis that helium storage on grain interfaces is significant in fine grained Josephine peridotites.

### 5.3.3. No major influence of dislocation and sub-grain boundaries

Based on neon and helium concentrations in oceanic mylonites and ultramylonites, Kurz et al. (2009) suggested that noble gases may be stored on subgrain boundaries and crystal defect sites. Ductile deformation of olivine in the dislocation creep regime creates dislocations, while recrystallization can remove such defects, depending on the mechanism of recrystallization. Deformation also results in the formation of subgrain boundaries, which are alignments of dislocations that create an angular mismatch in the crystal lattice of < 10° and eventually form grain boundaries. Petrographically, subgrain boundaries are observed as undulatory extinction under cross-polarized light.

In shear zone A, one test for the role of crystal defects as host sites for noble gases is to measure the abundance of dislocations. In olivine, dislocations can be imaged by oxidizing samples (Kohlstedt et al., 1976). However, peridotites from outside shear zone A were already deformed: olivine grains have sub-grain boundaries and a pre-existing lattice preferred orientation (Warren et al., 2008), which is interpreted as reflecting high temperature (> 1200 °C) flow in the asthenosphere. The decoration of olivine in four thin sections confirmed that even the sample with the lowest helium concentration (JP10M14) has a complex dislocation structure (Fig. 8) and sub-grain boundaries. In such low strain samples, dislocations were probably produced prior to shear zone formation, during the flow that produced the olivine LPO.

No significant variation in dislocation density among the four decorated samples was observable by petrographic microscope (i.e., any variations must be < 10%), with dislocation densities possibly being lower in the most deformed sample. In contrast, the helium concentration in sample JP10M08 is a factor of 5 higher than in sample JP10M14. Similarly, JP10M08 appears to have lower abundances of subgrain boundaries due to recrystallization. Therefore, dislocations and sub-grain boundaries are not the cause for the increased helium storage in the most deformed Josephine sample. However, they cannot be ruled out as major storage sites for noble gases until dislocation-free samples can be compared to dislocation-bearing samples from the same setting.

5.3.4. Helium diffusion processes and deformation

Diffusion data in mantle minerals are limited, and the diffusive behavior of helium in rocks is not well understood, especially for ductilely deformed samples (Baxter, 2010). The only existing olivine diffusion experiments at magmatic temperatures (700–1400 °C) were performed by Hart (1984) and Trull and Kurz (1993). These studies reported typical helium diffusion coefficients in olivine of $\sim 10^{-12}$ cm^2/s at 1000 °C, and high activation energies (502 and 420 kJ/mol respectively). This olivine diffusion coefficient implies that equilibration across the 16 cm distance between the two closest-spaced samples would require at least 8 Myr. Once the Josephine was emplaced around 150 Ma (Saleeby et al., 1982), the temperature dropped below ~ 500 °C and diffusion processes became negligible. However, low temperature (150–850 °C) experiments have yielded lower activation energies and higher diffusivities (Futagami et al., 1993; Shuster and Farley, 2004). Extrapolation

A

100 μm

B

100 μm
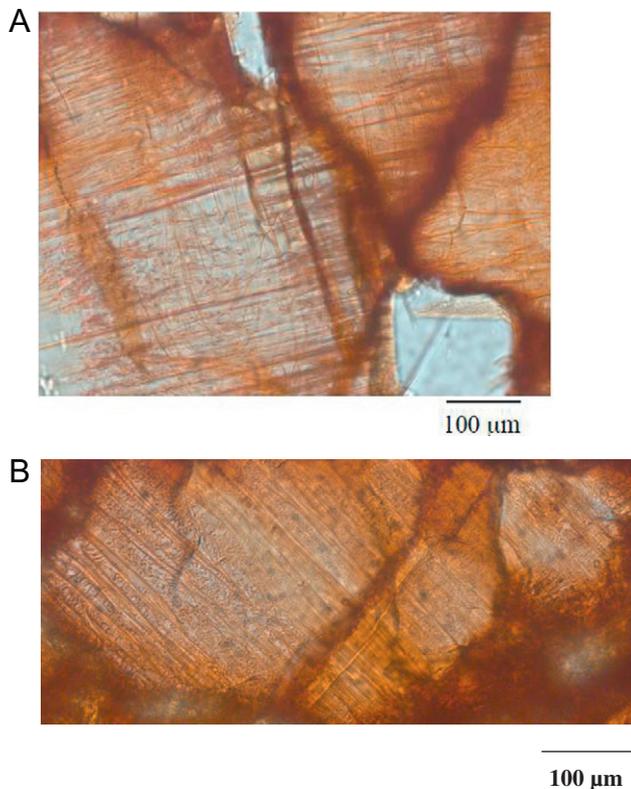
Fig. 8. Oxidized dislocations in olivine grains from sample JP10M14 (A) and JP10M08 (B).

of these data to 1000 °C yields a much higher diffusion coefficient of $\sim 10^{-8}$ cm^2/s. Diffusive equilibration between the two closest-spaced samples would then require only ~ 800 yr. Additionally, with these low activation energies, diffusion processes would become negligible only below 350 °C. The temperature dependency of helium diffusivity in olivine may not obey a single Arrhenius relationship, which might reconcile the high and low temperature studies. The high temperature experimental data would then be most appropriate for samples in this study.

A reduction in diffusional loss is unlikely to be responsible for the high helium contents in the highest strained sample JP10M08. Indeed, even though ductile deformation has an effect on noble gas retentivity in minerals (Baxter, 2010), it is generally assumed that it *increases* the diffusional loss. This topic has been explored for argon diffusivity in micas and potassium feldspar (e.g., Dunlap and Kronenberg, 2001; Reddy et al., 1996, 1999, 2001; Mulch et al., 2002). Grain size reduction results in a decrease in the effective diffusive lengthscale. Plastic deformation may also enhance argon diffusivity (Reddy et al., 1996, 1999, 2001) but this may be negligible (Dunlap and Kronenberg, 2001; Mulch et al., 2002). Defects, such as dislocations, could participate in increasing argon diffusional loss (Mulch et al., 2002). In the Josephine samples, this effect is probably negligible, since the defect density seems approximately homogeneous across the shear zone. However, helium grain boundary storage might be an important control on diffusive behavior in these samples. Grain boundaries may increase apparent diffusivity, acting as "fast paths", but grain boundary diffusion data do not exist (Baxter, 2010).

5.4. Role of melt infiltration

Field studies of the Josephine Peridotite have shown that melting, melt extraction and melt addition were all important

processes in the petrogenesis of this area (Dick, 1976; Kelemen and Dick, 1995; Sundberg et al., 2010). Samples collected from outside of shear zone A include pyroxenite veins and dunites, which are thought to be related to various episodes of melt infiltration and melt extraction in the Josephine Peridotite (Himmelberg and Loney, 1973; Kelemen and Dick, 1995). In this model, the clinopyroxenite (JP10M05) represents a melt that was saturated in clinopyroxene. Thus, it is interesting that this sample has a helium concentration of 1550 nccSTP/g, which is eight times higher than clinopyroxene from the nearby harzburgite (JP10M04), which has 193 nccSTP/g. Additionally, the chromitite vein (JP10M01) has a whole rock helium concentration of 345 nccSTP/g, which is also 2.5 times higher than the whole rock concentration of 137 nccSTP/g for harzburgite JP10M04. Based on these preliminary data, melt infiltration and melt extraction/transport processes also had an important influence on helium concentrations in the Josephine Peridotite. In contrast, the isotopic ratios (crushing values) of all samples, both within and outside the shear zone, are indistinguishable within measurement uncertainty.

5.5. ^{3}He/^{4}He signature of the Josephine Peridotite

5.5.1. Absence of radiogenic component

The isotopic ratio obtained by crushing is constant for all the measurements: ^{3}He/^{4}He$=6.7 \pm 0.2$ Ra ($n=33$). Based on the assumptions that the radiogenic production ratio is ^{3}He/^{4}He$_{rad} < 0.1$ and that the mantle ratio is ^{3}He/^{4}He> 6.3, then the cosmogenic contribution is minor. Thus, helium from the Josephine Peridotite is dominantly of mantle origin, as is found in many arcs (Hilton et al., 2002; Dodson and Brandon, 1999). The helium isotopic signature was presumably acquired during residence of the peridotite in either the mantle wedge (fore-arc origin) or beneath the spreading ridge in a back-arc basin. None of the Josephine samples have a distinct radiogenic component, contrary to a study of peridotite xenoliths from the western USA (Dodson and Brandon, 1999) that displayed low ^{3}He/^{4}He (< 4.2 Ra) in a few samples, which were interpreted as evidence for mantle metasomatism.

The absence of any radiogenic helium isotopic signature in the 157 Myr old Josephine Peridotite is puzzling. The initial mantle ^{3}He/^{4}He is unknown for the Josephine Peridotite. However, closed-system calculations show that even assuming very high initial ^{3}He/^{4}He ratios requires very low Th and U contents. For instance, using the highest known present-day back arc value as an *upper limit* for initial ^{3}He/^{4}He, ~ 28 Ra from the Lau Basin (Lupton et al., 2009), the upper limits for uranium (U) and thorium (Th) concentrations calculated within this closed system would be < 0.25 and < 0.75 ppb, respectively. The radiogenic helium concentration would thus be < 8 nccSTP/g. In this closed-system calculation, the radiogenic production rate over 157 Myr was estimated using present day ^{4}He$_{total}=50$ nccSTP/g and ^{3}He/^{4}He$_{total}=6.7$, and assuming Th/U$=3$ (Gautheron and Moreira, 2002).

U and Th contents are low in peridotites, which makes the measurement difficult as they are close to the detection limit for most analytical techniques. For example, whole rock inductively-coupled plasma mass spectrometer measurements of the Josephine samples yielded Th of 28–45 ppb and U of 8–13 ppb (WSU Geoanalytical Lab, Table 1), with no increase in U and Th contents in sample JP10M08. In a compilation of analytical reference standards, Govindaraju (1994) estimated that peridotites have Th$=13$ ppb and U$=4.5$ ppb, higher than the Josephine upper limits if ^{4}He is derived by closed system evolution. Thus, the helium isotopic composition of the Josephine Peridotite highlights the absence of reliable measurements of U and Th in peridotites.

Alternatively, if the Th and U measurements in the Josephine whole rock samples are reliable, the lack of an apparent unradiogenic helium component could be explained by a recent process that added uranium and thorium.

Gautheron and Moreira (2002) also observed that the uranium content of the subcontinental mantle necessary to account for a closed system is very low. They suggested an alternative model, involving a helium flux from the underlying asthenosphere. This model involves transport of helium by melts and/or fluids. However, the lack of variation in ^{3}He/^{4}He among all samples in this study suggests that melt infiltration did not alter the isotopic composition of the Josephine Peridotite. Thus, unless another source of ^{3}He affected the isotopic composition of all the samples, this model does not explain the present helium isotopic signature of the Josephine Peridotite.

5.5.2. Mantle signature of helium from orogenic peridotites?

The vacuum crushing and melting protocols used in this study have been mostly used on young volcanic rocks, such as basalts (e.g., Kurz and Jenkins, 1981; Kurz, 1986, Kurz et al., 1990), and have not been widely applied to peridotites. Basaltic olivine phenocrysts usually contain fluid and/or melt inclusions that formed during rapid cooling (at ~ 1200 °C). The crushing protocols were developed to release helium from these inclusions.

Results from this study suggest that these methods are also applicable to peridotites, which cooled very slowly compared to volcanic rocks. Therefore, they contain very few inclusions, which are smaller than in basaltic phenocrysts (probably < 1 μm), and it is difficult to determine the site responsible for helium released during crushing of the peridotite samples. Almost no radiogenic helium appears to be released during crushing, based on the lack of a radiogenic component and the small fraction of helium released by crushing (4–13%). Moreover, cosmogenic helium appears to be released during the melting stage, based on the systematically higher ^{3}He/^{4}He ratio obtained by melting. Therefore, the ^{3}He/^{4}He ratio determined by crushing the peridotite samples probably yields the mantle source helium isotopic composition. The helium isotopic composition obtained from ultramafic xenoliths and basaltic phenocrysts from different continental volcanic provinces is relatively constant (^{3}He/^{4}He=6.1 $\pm$ 0.9, 114 measurements), and is interpreted to represent the subcontinental lithospheric mantle (Gautheron et al., 2002, 2005). It is noteworthy that the Josephine Peridotite has a very similar isotopic composition.

5.6. ^{3}He cosmogenic exposure age of the Josephine Peridotite

The relatively constant amount of ^{3}He in the shear zone A samples can be used to estimate the exposure age for the Josephine Peridotite. Using a sea level high latitude production rate of 116 atoms/g/yr, the cosmogenic ^{3}He abundances in shear zone A samples yield an average exposure age of 10 ± 1 Kyr (based on the methodology and scaling described by Kurz, 1986; Lal, 1991; Licciardi et al., 1999). The local paleoclimate context is not well constrained and these samples were not collected for this purpose. However, a nearby study in the northern Klamath-Siskiyou Mountains estimated that deglaciation occurred in this area around 11 Kyr (Briles et al., 2008). Rock glaciers and cirque moraines from the White Mountains (California) have been dated at 11 Kyr from ^{36}Cl surface exposure dating (Zreda and Philipps, 1995). Therefore, the exposure age determined for the Josephine Peridotite is approximately concordant with local glacial retreat from the last glacial maximum. This exposure age is extremely young compared with the ~ 157 Myr emplacement age of the Josephine Peridotite (Saleeby et al., 1982) and suggests that glacial erosion controls the exposure age.

6. Conclusions

The data presented here confirm that highly deformed upper mantle peridotites can have higher helium contents, as suggested by Kurz et al. (2009), Baxter et al. (2007), and Hiraga et al. (2004, 2007). The highest helium content occurs in the highest strained sample from the center of shear zone A in the Josephine Peridotite, which is also the finest-grained sample. The short spatial scale of the sampling in shear zone A, and the petrological and mineralogical homogeneity of the outcrop suggest that grain size is the main variable controlling the storage of helium among these peridotite samples. In contrast, no significant variation in dislocation density or subgrain boundaries is observed as a function of strain across the shear zone, as samples outside the shear zone had previously been deformed during upper mantle flow. Based on these observations, we propose that a component of helium is stored on grain boundaries, where grain boundaries are considered to have a finite volume. Grain size reduction, such as observed in sample JP10M08, results in higher whole rock helium concentrations due to a significant increase in grain boundary volume. The increase in the helium concentration and relative grain boundary volume occurs over a length scale of less than 50 cm. The relative increase in helium concentration directly scales with the relative increase in grain boundary volume with respect to grain matrix volume.

The present data indicate that the helium isotopic signature of the Josephine Peridotite is ^{3}He/^{4}He=6.7 $\pm$ 0.2 Ra (n=33). This value falls within the low end of the range reported for mid-ocean ridge basalts, suggesting that the Josephine is dominated by mantle-derived helium. Analysis of four samples outside shear zone A suggests that mineralogy and melt infiltration processes can also control helium concentrations. Despite the Jurassic age of this massif, radiogenic helium could not be detected, suggesting low concentrations of Th and U in the Josephine. Cosmogenic ^{3}He abundances suggest a recent exposure age of 10 Kyr, probably related to exposure following the last glacial maximum.

References

Baxter, E.F., Asimow, P.D., Farley, K.A., 2007. Grain boundary partitioning of Ar and He. Geochim. Cosmochim. Acta 71, 434–451.

Baxter, 2010. Diffusion of noble gases in minerals. Rev. Mineral. Geochem. 72, 509–557.

Boudier, F., Ceuleneer, G., Nicolas, A., 1988. Shear zones, trusts and related magmatism in the Oman ophiolite: initiation of thrusting on an oceanic ridge. Tectonophysics 151, 275–296.

Briles, C.E., Whitlock, C., Bartlein, P.J., Higuera, P., 2008. Regional and local controls on postglacial vegetation and fire in the Siskiyou Mountains, Northern California, USA. Paleogeogr. Paleoclimatol. Paleoecol. 265, 159–169.

deMartin, B., Hirth, G., Evans, B., 2004. Experimental constraints on thermal cracking of peridotites at oceanic spreading centers. in: German, C.R., Jin, L., Parson, L.M. (Eds.), Mid-Ocean Ridges: Hydrothermal Interactions Between the Lithosphere and Oceans, Geophysical Monograph Series, vol. 148. American Geological Union, Washington D.C., pp. 167–185.

Dick, H.J.B., 1976. The Origin and Emplacement of the Josephine Peridotite of Southwestern Oregon. Ph.D. Thesis, Yale University.

Dick, H.J.B., 1977. Partial melting in the Josephine Peridotite I, the effect on mineral composition and its consequence for geobarometry and geothermometry. Am. J. Sci. 277, 801–822.

Dodson, A., Brandon, A.D., 1999. Radiogenic helium in xenoliths from Simcoe, Washington, USA: implications for metasomatic processes in the mantle wedge above subduction zones. Chem. Geol. 160, 371–385.

Drury, M.R., 2005. Dynamic Recrystallization and Strain Softening of Olivine Aggregates in the Laboratory and the Lithosphere. Special Publications. Geological Society, London, vol. 243, pp. 143–158.

Dunlap, W.J., Kronenberg, A.K., 2001. Argon loss during deformation of micas: constraints from laboratory experimental data. Contrib. Mineral. Petrol. 141, 174–185.

Evans, A.G., 1978. Microfracture from thermal expansion anisotropy-I. Single phase systems. Acta Metall. 26, 1845–1853.

Futagami, T., Ozima, M., Nagai, S., Aoki, Y., 1993. Experiments on thermal release of implanted noble gases from minerals and their implication for noble gases in lunar soils. Geochim. Cosmochim. Acta 57, 3177–3194.

Gautheron, C., Moreira, M., 2002. Helium signature of the subcontinental mantle. Earth Planet. Sci. Lett. 199, 39–47.

Gautheron, C., Moreira, M., Allegre, C., 2005. He, Ne, and Ar composition of the European lithospheric mantle. Chem. Geol. 217, 97–112.

Graham, D.W., 2002. Mid-ocean ridge and ocean island basalts: characterization of mantle source reservoirs. Noble Gases Geochem. Cosmochem. Rev. Mineral. Geochem. 47, 247–305.

Govindaraju, K., 1994. Compilation of working values and sample description for 383 geostandards. Geostand. Newslett. 18, 1–158.

Harding, D.J., 1988. Josephine Peridotite Tectonites: A Record of Upper-Mantle Plastic Flow (Klamath Mountains, Oregon). Ph.D. Thesis, Cornell University.

Harper, G.D., 1984. The Josephine ophiolite, Northwestern California. Geol. Soc. Am. Bull. 95, 1009–1026.

Harper, G.D., Saleeby, J.B., Heizler, M., 1994. Formation and emplacement of the Josephine ophiolite and the Nevadan orogeny in the Klamath mountains, California–Oregon: U/Pb zircon and 40Ar/39Ar geochronology. J. Geophys. Res. 99, 4293–4321.

Harper, G.D., 2003. Fe–Ti basalts and propagating-rift tectonics in the Josephine Ophiolite. Geol. Soc. Am. Bull. 115, 771–787.

Hart, S.R., 1984. Helium diffusion in olivine. Earth Planet. Sci. Lett. 70, 297–302.

Hilton, D., Fischer, T.P., Marty, B., 2002. Noble gases and volatile recycling at subduction zones. Noble Gases Geochem. Cosmochem. Rev. Mineral. Geochem. 47, 319–362.

Himmelberg, G.R., Loney, R.A., 1973. Petrology of the Vulcan Peak alpine-type peridotite, southwestern Oregon. Geol. Soc. Am. Bull. 84, 1585–1600.

Hiraga, T., Anderson, I.M., Zimmerman, M., Mei, S., Kohlstedt, D.L., 2002. Structure and chemistry of grain boundaries in deformed, olivine+basalt and partially molten lherzolite aggregates: evidence of melt-free grain boundaries. Contrib. Mineral. Petrol. 144, 163–175.

Hiraga, T., Anderson, I.M., Kohlstedt, D.L., 2003. Chemistry of grain boundaries in mantle rocks. Am. Mineral. 88, 1015–1019.

Hiraga, T., Anderson, I.M., Kohlstedt, D.L., 2004. Grain boundaries as reservoirs of incompatible elements in the Earth's mantle. Nature 427, 699–703.

Hiraga, T., Hirschmann, M.M., Kohlstedt, D.L., 2007. Equilibrium interface segregation in the diopside-forsterite system II: applications of interface enrichment to mantle geochemistry. Geochim. Cosmochim. Acta 71, 1281–1289.

Hiraga, T., Kohlstedt, D.L., 2009. Systematic distribution of incompatible elements in mantle peridotite: importance of intra- and inter-granular melt-like components. Contrib. Mineral. Petrol. 158, 149–167.

Hirth, G., Kohlstedt, D.L., 2003. Rheology of the upper mantle and the mantle wedge: a view from the experimentalists. in: Eiler, J. (Ed.), The Subduction Factory. Geophysical Monograph, vol. 138. American Geophysical Union, pp. 83–105.

Jaroslow, G.E., Hirth, G., Dick, H.J.B., 1996. Abyssal peridotite mylonites: implications for grain-size sensitive flow and strain localization in the oceanic lithosphere. Tectonophysics 256, 17–37.

Kelemen, P.B., Dick, H.J.B., 1995. Focused melt flow and localized deformation in the upper mantle: juxtaposition of replacive dunite and ductile shear zones in the Josephine Peridotite, SW Oregon. J. Geophys. Res. 100, 423–438.

Kohlstedt, D.L., Goetze, C., Durham, W.B., Vander Sande, J., 1976. New technique for decorating dislocations in olivine. Science, New Series 191, 1045–1046.

Kumagai, H., Dick, H.J.B., Kaneoka, I., 2003. Noble gas signature of abyssal gabbros and peridotites at an Indian Ocean core complex. Geochem. Geophys. Geosyst. 4, 9107, http://dx.doi.org/10.1029/2003GC000540.

Kumagai, H., Sato, K., McCaig, A., Abe, N., Dick, H.J.B., 2008. Correspondences of helium isotope compositions between gabbros and abyssal peridotites with basalts: a view for heterogeneity inferred from the volcanics in uppermost mantle. Geochim. Cosmochim. Acta 72, 502.

Kurz, M.D., Jenkins, W.J., 1981. The distribution of helium in oceanic basalt glasses. Earth Planet. Sci. Lett. 53, 41–54.

Kurz, M.D., 1986. Cosmogenic helium in a terrestrial igneous rock. Nature 320, 435–439.

Kurz, M.D., Colodner, D., Trull, T.W., Moore, R.B., O'Brien, K., 1990. Cosmic ray exposure dating with in-situ produced cosmogenic ^{3}He: results from young Hawaiian lava flows. Earth Planet. Sci. Lett. 97, 177–189.

Kurz, M.D., Curtice, J., Lott, D.E., Solow, A., 2004. Rapid helium isotopic variability in Mauna Kea shields lavas from the Hawaiian Scientific Drilling Project. Geochem. Geophys. Geosyst. 5 , http://dx.doi.org/10.1029/2002GC000439, Q04G14.

Kurz, M.D., Warren, J.M., Curtice, J., 2009. Mantle deformation and noble gases: helium and neon in oceanic mylonites. Chem. Geol. 266, 10–18.

Lal, D., 1991. Cosmic ray labeling of erosion surfaces: in situ nuclides production rates and erosion models. Earth Planet. Sci. Lett. 104, 424–439.

Licciardi, J.M., Kurz, M.D., Clark, P.U., Brook, E.J., 1999. Calibration of cosmogenic ^{3}He production rates from Holocene lava flows in Oregon, USA, and effects on the Earth's magnetic field. Earth Planet. Sci. Lett. 172, 261–271.

Loney, R.A., Himmelberg, G.R., 1976. Structure of the Vulcan Peak alpine-type peridotite, Southwestern Oregon. Geol. Soc. Am. Bull. 87, 259–274.

Lupton, J.E., Arculus, R.J., Greene, R.R., Evans, L.J., Goddard, C.I., 2009. Helium isotope variations in seafloor basalts from the Northwest Lau Backarc Basin: mapping the influence of the Samoan hotspot. Geophys. Res. Lett. 36, L17313, http://dx.doi.org/10.1029/2009GL039468.

Mulch, A., Cosca, M.A., Handy, M.R., 2002. In situ UV-laser 40Ar/39Ar geochronology of a micaceous mylonite: an example of defect-enhanced argon loss. Contrib. Mineral. Petrol. 142, 738–752.

Pinilla, C., Davis, S.A., Scott, T.B., Allan, N.L., Blundy, J.D., 2012. Interfacial storage of noble gases and other trace elements in magmatic systems. Earth Planet. Sci. Lett. 319–320, 287–294.

Ramsay, J.G., Graham, R.H., 1970. Strain variations in shear belts. Can. J. Earth Sci. 7, 786–813.

Reddy, S.M., Kelley, S.P., Wheeler, J., 1996. A 40Ar/39Ar laser probe study of micas from the Sezia Zone, Italian Alps: implications for metamorphic and deformation histories. J. Metamorphic Geol. 14, 493–508.

Reddy, S.M., Potts, G.J., Kelley, S.P., 2001. 40Ar/39Ar ages in deformed potassium feldspar: evidence of microstructural control on Ar isotope systematic. Contrib. Mineral. Petrol. 141, 186–200.

Reddy, S.M., Potts, G.J., Kelley, S.P., Arnaud, N.O., 1999. The effect of deformation-induced microstructures on intragrain 40Ar/39Ar ages in potassium feldspar. Geology 27, 363–366.

Saleeby, J.B., Harper, G.D., Snoke, A.D., Sharp, W.D., 1982. Time relations and structural-stratigraphic patterns in ophiolite accretion, west central Klamath Mountains. California. J. Geophys. Res. 87, 3831–3848.

Shuster, D.L., Farley, K.A., 2004. ^{4}He/^{3}He thermochronometry. Earth Planet. Sci. Lett. 217, 1–17.

Skemer, P., Warren, J.M., Kelemen, P.B., Hirth, G., 2010. Microstructural and rheological evolution of a mantle shear zone. J. Petrol. 51, 43–53.

Sundberg, M., Hirth, G., Kelemen, P.B., 2010. Trapped melt in the Josephine Peridotite: implications for permeability and melt extraction in the upper mantle. J. Petrol. 51, 185–200.

Terwilliger, C.D., Chiang, Y-M., 1995. Size dependent solute segregation and total solubility in ultrafine polycrystals: Ca in TiO$_2$. Acta Metall. Mater. 43, 319–328.

Trull, T., Kurz, M.D., 1993. Experimental measurements of ^{3}He and ^{4}He mobility in olivine and clinopyroxene at magmatic temperatures. Geochim. Cosmochim. Acta 57, 1313–1324.

Underwood, E.E., 1970. Quantitative Stereology. Addison-Wesley, Reading, Massachusetts.

Warren, J.M., Hirth, G., Kelemen, P.B., 2008. Evolution of lattice preferred orientation during simple shear in the mantle. Earth Planet. Sci. Lett. 272, 501–512.

Ye, X., Tao, M., Yu, C., Zhang, M., 2007. Helium and neon isotopic compositions in the ophiolites from the Yarlung Zangbo River, Southwestern China: the information from deep mantle. Sci. Chin. D 50 (6), 801–812.

Zreda, M.G., Philipps, F.M., 1995. Insights into alpine moraine development from cosmogenic 36Cl buildup dating. Geomorphology 14, 149–156.